SUBMITTED TO ASTROPHYS. J.
Preprint typeset using LaTeX style emulateapj v. 5/2/11
1

arXiv:1405.4173v1 [astro-ph.SR] 16 May 2014

May 19, 2014

OH^+ IN ASTROPHYSICAL MEDIA: STATE-TO-STATE FORMATION RATES, EINSTEIN COEFFICIENTS AND INELASTIC COLLISION RATES WITH HE

SUSANA GÓMEZ-CARRASCO [a], BENJAMIN GODARD[b], FRANÇOIS LIQUE[c], NIYAZI BULUT[d], JACEK KŁOS[e], OCTAVIO RONCERO[f,1], ALFREDO AGUADO[g], F. JAVIER AOIZ[h], JESÚS F. CASTILLO[h], JAVIER R. GOICOECHEA[i], MIREYA ETXALUZE[i] AND JOSÉ CERNICHARO[i].

(a) Facultad de Química, Unidad Asociada CSIC-USAL, Universidad de Salamanca, Spain.
(b) LERMA, CNRS UMR 8112, Observatoire de Paris, Meudon, France
(c) LOMC - UMR 6294, CNRS-Université du Havre, 25 rue Philippe Lebon, BP 540, 76058, Le Havre, France
(d) Department of Physics, Firat University, 23169 Elazığ, Turkey
(e) Department of Chemistry and Biochemistry, University of Maryland, College Park, MD 20742-2021, USA
(f) Instituto de Física Fundamental (IFF-CSIC), C.S.I.C., Serrano 123, 28006 Madrid, Spain.
(g) Facultad de Ciencias, Unidad Asociada de Química-F ísica Aplicada CSIC-UAM, Universidad Autónoma de Madrid, Spain
(h) Departamento de Química Física I, Unidad Asociada de Química-Física CSIC-UCM, Facultad de Química, Universidad Complutense de Madrid, Spain and
(i) Instituto de Ciencia de Materiales (ICMM-CSIC), C.S.I.C., Sor Juana Inés de la Cruz, 3, Cantoblanco, 28049 Madrid, Spain

Submitted to Astrophys. J.

ABSTRACT

The rate constants required to model the OH^+ observations in different regions of the interstellar medium have been determined using state of the art quantum methods. First, state-to-state rate constants for the $H_2(v = 0, J = 0, 1)$+ $O^+(^4S) \rightarrow$ H + $OH^+(X^3\Sigma^-, v', N)$ reaction have been obtained using a quantum wave packet method. The calculations have been compared with time-independent results to asses the accuracy of reaction probabilities at collision energies of about 1 meV. The good agreement between the simulations and the existing experimental cross sections in the $0.01-1$ eV energy range shows the quality of the results. The calculated state-to-state rate constants have been fitted to an analytical form. Second, the Einstein coefficients of OH^+ have been obtained for all astronomically significant ro-vibrational bands involving the $X^3\Sigma^-$ and/or $A^3\Pi$ electronic states. For this purpose the potential energy curves and electric dipole transition moments for seven electronic states of OH^+ are calculated with *ab initio* methods at the highest level and including spin-orbit terms, and the rovibrational levels have been calculated including the empirical spin-rotation and spin-spin terms. Third, the state-to-state rate constants for inelastic collisions between He and $OH^+(X^3\Sigma^-)$ have been calculated using a time-independent close coupling method on a new potential energy surface. All these rates have been implemented in detailed chemical and radiative transfer models. Applications of these models to various astronomical sources show that inelastic collisions dominate the excitation of the rotational levels of OH^+. In the models considered the excitation resulting from the chemical formation of OH^+ increases the line fluxes by about 10 % or less depending on the density of the gas.

1. INTRODUCTION

Light hydrides represent the very first step of interstellar chemistry. They start reaction cycles that initiate the formation of complex molecules and are therefore at the root of the molecular richness observed for decades in all interstellar environments. In addition, because of the diversity of their formation and excitation pathways, their rotational lines offer powerful diagnostics of the physical and chemical processes at play in the interstellar medium (ISM).

These investigations have recently been deepened by the Herschel satellite which opened the spectral domain of hydrides absorption and emission that was not accessible to us before due to the large opacity of the Earth atmosphere. Indeed, many light hydrides (e.g. CH, CH^+, HF, HCl, OH^+, H_2O, NH, SH^+) have been observed, some of them for the first time, in different types of interstellar and circumstellar regions (e.g. Benz et al. 2010; Cernicharo et al. 2010; Hily-Blant et al. 2010; Gerin et al. 2010; Naylor et al. 2010; van Dishoeck et al. 2011; Neufeld et al. 2011; Godard et al. 2012; Spoon et al. 2013).

Among all the hydrides detected to date, the hydroxyl cation OH^+ is particularly interesting, not only because it initiates the oxygen chemistry, but also because its abundance could be a valuable tracer of cosmic ray and X-ray ionization rates (Gerin et al. 2010; Hollenbach et al. 2012; González-Alfonso et al. 2013). First detected in absorption in the diffuse medium (Wyrowski et al. 2010; Gerin et al. 2010; Neufeld et al. 2010; Krelowski et al. 2010; Porras et al. 2014), OH^+ has then been also observed in absorption and emission in a variety of interstellar and circumstellar environments including hot and dense photodissociation regions (PDR) (van der Tak et al. 2013; Pilleri et al. 2014), galactic center clouds (Etxaluze et al. 2013; Goicoechea et al. 2013), planetary nebulae (Etxaluze et al. 2014; Aleman et al. 2014) and the nuclei of active galaxies (van der Werf et al. 2010; González-Alfonso et al. 2013) . These observations need to be interpreted both in terms of chemistry and excitation processes for which important properties of the OH^+ molecule are still lacking.

The chemistry of OH^+ in molecular clouds is rather well understood. As the depth into the cloud increases and the far ultraviolet (FUV) flux decreases, the formation of OH^+ successively follows two different pathways (Hollenbach et al. 2012). At the border of diffuse clouds where most of the Hydrogen is atomic, the production of OH^+ proceeds through

$$H \xrightarrow{CR} H^+ \xrightarrow{O} O^+ \xrightarrow{H_2} OH^+, \quad (1)$$

[1] e-mail: octavio.roncero@csic.es

being initiated by the ionization of atomic Hydrogen by cosmic rays (CR). Conversely, deeper in the cloud where most of the Hydrogen is molecular, the production of OH^+ proceeds through

$$H_2 \xrightarrow{CR} H_2^+ \xrightarrow{H_2} H_3^+ \xrightarrow{O} OH^+. \quad (2)$$

As a result, the abundance of OH^+ predicted by chemical models displays two peaks whose position and magnitude depend on the ratio of the incident UV radiation field and the gas density (Hollenbach et al. 2012).

On the other hand and because of the lack of theoretical and experimental data, uncertainties remain on the processes involved in populating the rotational levels of OH^+. Firstly, these levels might be excited by inelastic collisions. In the cold ISM, the most abundant species are H_2 and He. In warmer regions such as diffuse, translucent clouds or PDRs, collisions with electrons and atomic Hydrogen should also be taken into account. Secondly, since OH^+ is observed in hot PDRs illuminated by strong infrared (IR) and UV radiation fields, its rotational levels might be sensitive to the radiative pumping of its vibrational and electronic states followed by radiative decay. Indeed, these mechanisms have been found to dominate the excitation of many species (e.g. H_2O, HNC, NH_3, H_2, CO, CH^+) in molecular clouds and circumstellar envelopes (e.g. González-Alfonso & Cernicharo 1999; Agúndez & Cernicharo 2006; Agúndez et al. 2008; Troutman et al. 2011; Godard & Cernicharo 2013). At last, since OH^+ is a very reactive molecule it was assumed that it is destroyed before inelastic collisions may take place and it has been proposed that its rotational population is governed by its chemical formation (van der Tak et al. 2013). For instance, it has recently been shown that chemical state-to-state formation pumping plays a major role in the excitation of several molecules such as CH^+ in hot and dense PDRs, planetary nebulae and circumstellar disks (Nagy et al. 2013; Godard & Cernicharo 2013; Zanchet et al. 2013b,a).

The purpose of this paper is to provide the excitation rates of OH^+ through radiative pumping, inelastic collisions, and reactive collisions in order to improve the reliability of chemical and radiative transfer models applied to astrophysical environments. It is organized as follows: in Sect. II, we study the excitation of OH^+ during its chemical formation via $O^+(^4S)$ + $H_2(v, J) \rightarrow OH^+(X^3\Sigma^-, v', N)$ + H. Up to now, only total reaction cross sections and rate constants have been obtained, both experimentally (Burley et al. 1987) and theoretically using quasi-classical trajectory (QCT) calculations (Martínez et al. 2005), time independent calculations with hyperspherical coordinates (TI), and wave packet (WP) methods (Martínez et al. 2006; Xu et al. 2012) using the adiabatic ground electronic state potential energy surface (PES) of Martínez et al. (2004); in Sect. III, we focus on the radiative pumping of the vibrational and electronic levels of OH^+ by infrared and UV photons. In a previous study, de Almeida & Singh (1981) have reported the absolute oscillator strengths for several vibrational states of the OH^+ $(X^3\Sigma^-, A^3\Pi)$ system based on the radiative lifetimes measured by Brzozowski et al. (1974) and the ultraviolet emission spectra of OH^+ observed by Merer et al. (1975). To extend these results to higher J and v values, we compute here the *ab initio* potential energy curves of the $OH^+(X^3\Sigma^-, A^3\Pi)$ band system; in Sect. IV, we investigate the excitation of OH^+ by inelastic collisions with He and use the results as a model for collisions with H and H_2. So far, previous studies have only reported excitation rates by electron impact (Schöier et al. 2005; van der Tak et al. 2013). We compute here the interaction potential of the He-$OH^+(X^3\Sigma^-)$ system and perform scattering calculations in order to derive for the first time the associated collisional rate constants; finally, we discuss, in Sects. V and VI, the implication of all these results on the modeling of astrophysical environments and the interpretation of observations.

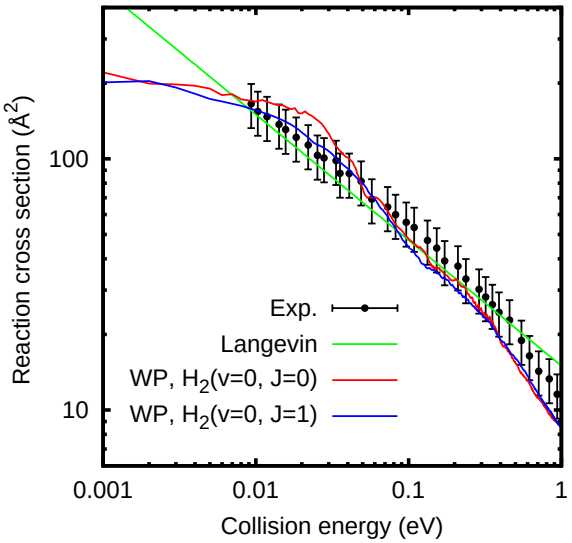

FIG. 1.— Total reaction cross section for the $H_2(v, = 0, J = 0, 1)$+O^+ collisions as a function of collision energy. The experimental results are taken from Burley et al. (1987). The Langevin results come from the typical Lagevin model $\sigma(E) = A/\sqrt{E}$, with A=15 Å^2 eV$^{1/2}$.

For reasons of clarity and comprehensibility of the manuscript, the details of the reactive collisions are given in Appendix A together with the list of parameters obtained to fit the state-to-state rate constants; the *ab initio* details for the calculation of the 7 electronic states of OH^+ and the Einstein coefficients are described in Appendix B; the calculation of the PES built in this work for the He + $OH^+(X^3\Sigma^-)$ is described in Appendix C; finally, the time-independent calculation details of the He + $OH^+(X\Sigma^-)$ inelastic collisions are given in Appendix D.

2. REACTIVE COLLISION SIMULATIONS

The state-to-state rate constants for the $O^+(^4S)$ + $H_2(v, J)$ $\rightarrow$ $OH^+(X^3\Sigma^-)$ + H reaction have been calculated using a time dependent WP method (find further details in Appendix A) on the ground electronic state PES of Martínez et al. (2004). The details of the computations are described in Appendix A together with the convergence analysis and comparison with results obtained using time-independent methods.

$OH^+(X^3\Sigma^-)$ products are treated in Hund's case (b), and the total diatomic angular momentum is $\mathbf{J} = \mathbf{N} + \mathbf{S}$, with $\mathbf{N}$ being the total rotational angular momentum and $\mathbf{S}$ the total electronic spin. In the simulation of the reactive collision rates, the effect of the electronic spin is neglected. Under this approximation, several alternatives are possible to determine the population of the three $F_1(J = N + 1)$, $F_2(J = N)$ and $F_3(J = N - 1)$ levels. One possibility would be to consider the three levels equally populated. However, we shall assume here that the population of each F_i sublevels is proportional to the degeneracy $(2J + 1)$.

The total reaction integral cross section (ICS) is obtained

after partial wave summation as described in Appendix A, and is compared in Fig. 1 with both the experimental results of Burley et al. (1987) and the results obtained using the Langevin model (Langevin 1905; Gioumousis & Stevenson 1958). The Langevin model is in good agreement with the experimental results, although slightly lower for collision energies < 0.5 eV. Burley et al. (1987) attributed this small difference to the simplicity of the Langevin model, which only takes into account the distance between reactants, but not the anisotropy of the reaction.

The ICS results for $J = 0$ and 1 are very close to each other, except for energies below 0.04 eV where the cross section for $J = 0$ is slightly higher. The agreement with the experimental data is very good, nearly always inside the experimental error bars. It is interesting that for $E < 0.01$ eV the calculated cross section deviates from the simple Langevin model. These small inaccuracies affect more notoriously to low collision energies. For energies above 0.3-0.4 eV, the WP results become slightly below the experimental error bars, probably due to small inaccuracies of the PES. The experimental results also show a change of the energy dependence at these energies with respect to the pure Langevin model. It can be concluded that the simulated cross sections are in very good agreement with the available experimental results, and can thus be used to estimate rate constants.

The rate constants in the 50-5000 K temperature range are obtained by numerical integration of the state-to-state cross sections, in the 1meV-1.5eV energy range . The total and vibrationally resolved rate constants are shown in Fig. 2. The agreement with the only experimental value of Burley et al. (1987) is good. The rates for $v' = 0$ and 1 are both significant over the whole range of temperatures considered, while the rates to OH^+ products in $v' > 1$ are negligible. The results derived for $H_2(v = 0, J = 0, 1)$ are within the error bars of the experimental value obtained by Burley et al. (1987) at room temperature. The total rates show a slight decrease with increasing temperature. This departure from a pure Langevin behavior is due to the long range behaviour of the PES, which is not isotropic as assumed in the simple mono-dimensional Langevin model.

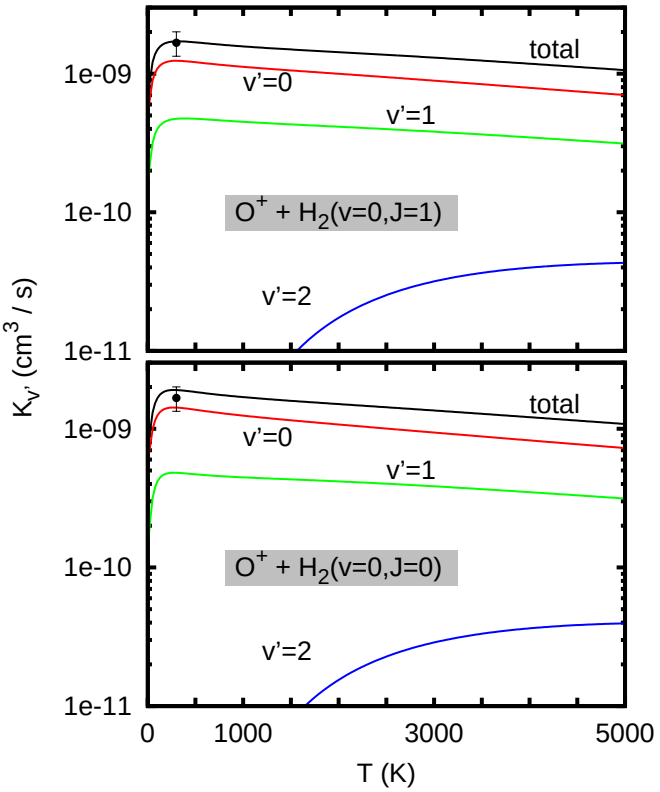

FIG. 2.— Total and vibrationally resolved rate constants for the $O^+ + H_2(v, = 0, J = 0, 1)$ collisions as a function of translational temperature. The experimental result of 1.67 10^{-9} cm^3/s is taken from Burley et al. (1987).

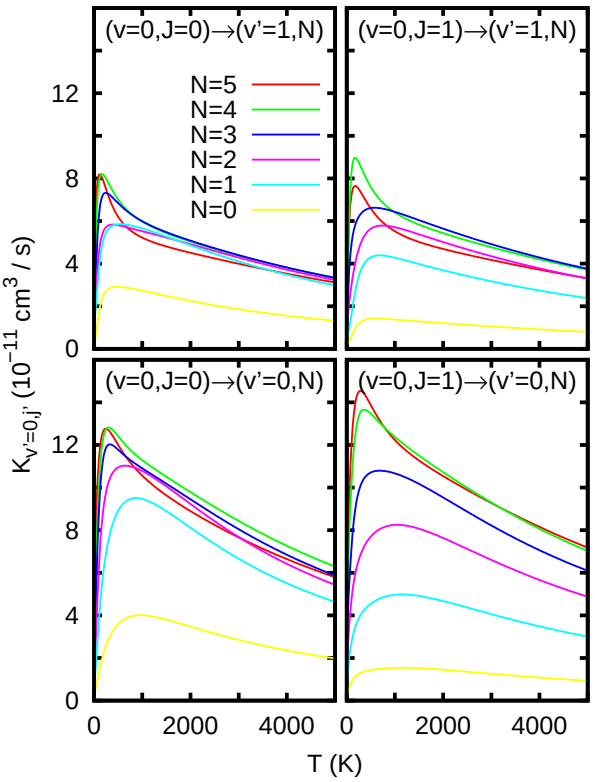

FIG. 3.— State-to-state rate constants for the $H_2(v, = 0, J = 0, 1)$+$O^+ \rightarrow OH^+(X^3\Sigma^-, v' = 0, 1, N)$ + H collisions as a function of translational temperature, with the quantum numbers being specified in each panel.

The rotationally resolved state-to-state rate constants are shown in Fig. 3, for initial rotational states of H_2, $J = 0$ (left panels) and $J = 1$ (right panels), and final vibrational states of OH^+, $v' = 0$ (bottom panels) and $v' = 1$ (top panels). The rates increase with increasing N, reaching a maximum at about $N = 6$ or 7, indicating that reactive collisions between O^+ and H_2 proceeds through a significant energy transfer in the excited states of the product OH^+. In fact, for initial $H_2(J = 1)$ the final $OH^+(N)$ products seem to be more excited by just one rotational quantum. The rates for $v' = 1$ are approximately 2/3 of those obtained for $v' = 0$ and show similar behaviors.

For $v' = 0$ and $N < 16$, the reaction has no threshold. However, at low temperatures, the rates for low N are nearly zero, increasing rapidly with temperature, reaching a maximum at about 300-800 K and decreasing again afterwards, so that at high temperatures the rates for all N become rather similar. For $v' = 0$ and $N > 16$, there is an energy threshold and the rates increase monotonously with increasing temperature. In the case of $v' = 1$, the behaviour is similar but the threshold appears at $N \approx 8$.

The state-to-state rate constants have been fitted as described in Appendix A and the parameters obtained are listed in Table 3.

3. EINSTEIN COEFFICIENTS FOR $OH^+(X^3\Sigma^-, A^3\Pi)$

In the previous section, the $H_2 + O^+(^4S) \rightarrow H+OH^+(X^3\Sigma^-)$ reaction has been studied in the ground adiabatic electronic state, without considering electronic spin. In this section we study the transitions between the X and A electronic states of OH^+. To do so it is important to consider that the total angular momentum of OH^+ is $\mathbf{J} = \mathbf{N} + \mathbf{S}$, with $\mathbf{N} = \mathbf{R} + \mathbf{L}$ where $\mathbf{R}$ is the rotational angular momentum, and $\mathbf{L}$ and $\mathbf{S}$ are the electronic orbital and spin angular momenta, respectively.

Seven electronic states of OH^+ have been calculated to describe properly the dissociation asymptotes of $OH^+(X^3\Sigma^-, A^3\Pi)$ as described in Appendix B. The potential energy curves are displayed in the top panel of Fig. 4. The dipole moments of the $X^3\Sigma^-$ ground state and the $A^3\Pi$ excited state along with the their transition dipole moments are displayed in the bottom panel of Fig. 4. In the following we focus on the $X^3\Sigma^-$ and $A^3\Pi$ states only.

The ultraviolet $A^3\Pi - X^3\Sigma^-$ emission spectra of OH^+ was studied by Merer et al. (1975). After including the spin-spin and spin-rotation terms and the Λ-doubling of the $A^3\Pi$ state due to the $A^1\Delta$ state, the deperturbed potential energy curves were obtained. The equilibrium distances for $X^3\Sigma^-$ and $A^3\Pi$ states in Table 8 of Merer et al. (1975) are $R_e = 1.028$ and 1.135Å respectively, in good agreement with the values of 1.0284 and 1.1356 Å obtained here. Merer et al. (1975) found a vertical excitation energy of $T_e = 28438.55$ cm^{-1} while here a value of 28522.65 cm^{-1} is obtained. Finally, the dissociation energies obtained here are 41900.0 and 13661.8 cm^{-1} for for $X^3\Sigma^-$ and $A^3\Pi$ states, respectively.

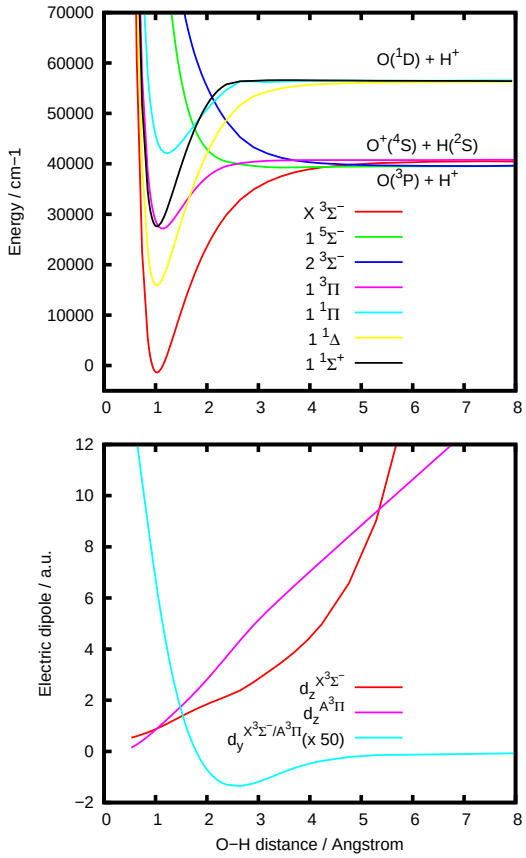

FIG. 4.— Top: Electronic states of the OH^+ cation. Bottom: Dipole moments and transition dipole moments between some of the electronic states. These results are obtained using the extrapolation up to complete basis set as explained in the text.

The details for the computation of the ro-vibrational states of OH^+ in the $X^3\Sigma^-$ and $A^3\Pi$ electronic states, and the Einstein coefficients, are described in Appendix B.

The radiative lifetimes of the $A^3\Pi_\Omega, v, J$ states are obtained as the inverse of the of sum of all possible $A^3\Pi_\Omega, v, J \rightarrow X^3\Sigma^-, v', J'$ transitions (Larsson 1983). Using the summation rule of the Hönl-London factors (Whiting & Nicholls 1974; Whiting et al. 1980) we define a vibrational lifetime (as done by Larsson 1983)

$$\tau_v = \left(\sum_{v'} \frac{1}{3\pi\epsilon_0 \hbar^4} \left(\frac{h\overline{\nu}}{c} \right)^3 \delta_{SS'} \left| M_{v;v'}^{J\Lambda S\alpha;J'\Lambda'S'\alpha'} \right|^2 \right)^{-1} \quad (3)$$

where $h\overline{\nu}$ is the average transition energy and the $M_{v;v'}^{J\Lambda S\alpha;J'\Lambda'S'\alpha'}$ are described in Appendix B. These radiative lifetimes are listed in Table 3 for $OH^+(A^3\Pi, v)$. There are two experimental studies reporting very different lifetimes for $OH^+(A^3\Pi, v = 0)$. Brzozowski et al. (1974) reported lifetimes for v between 850 and 1010 ns, obtained by averaging over rotational bands for particular $OH^+(A^3\Pi, v \rightarrow^3 \Sigma^-, v')$ bands. Later Möhlmann et al. (1978) reported a radiative lifetime for $OH^+(A^3\Pi, v = 0)$ of 2500 ns, in very good agreement with the results of the present work, but considerably longer than that reported previously (Brzozowski et al. 1974). These authors argued that this difference is originated from the effect of the pressure on the lifetimes in the case of long-range interactions present in charged gases. This makes necessary to carry out pressure dependent measurements to extrapolate to zero pressure to get reliable radiative lifetimes, as done by Möhlmann et al. (1978). We may therefore conclude, that our results are rather reliable. It should be noted that the Einstein coefficients obtained by de Almeida & Singh (1981) are based on the experimental radiative lifetimes of Brzozowski et al. (1974), and are therefore 2.5 times larger than those reported in this work.

TABLE 1
Radiative lifetimes, τ_v, for the vibrational states of the $OH^+(A^3\Pi, v)$ states calculated using Eq. (3).

v	τ_v (ns)
0	2524
1	2665
2	2820
3	3004
4	3233
5	3534
6	3960
7	4637
8	5961
9	9559
10	16118

4. COLLISIONAL EXCITATION OF $OH^+(X^3\Sigma^-)$ BY HE

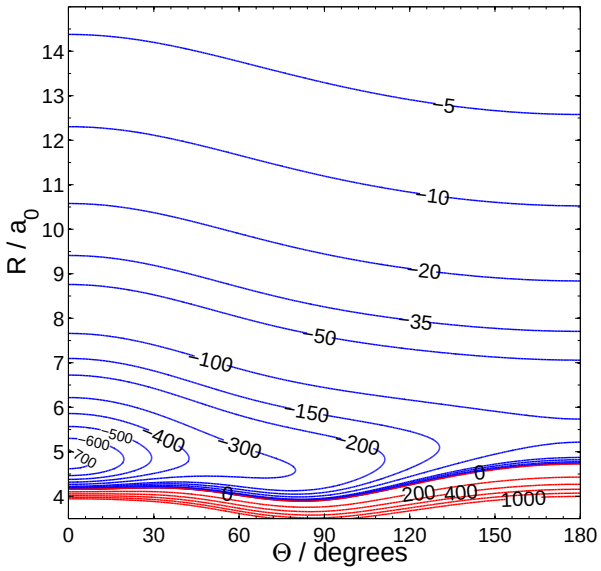

FIG. 5.— The contour plot of the vibrationally averaged $V(R, r, \theta)$ 3-D He-OH^+ PES over $\nu = 0$ wave function of the OH^+ cation. Contour labels are in cm^{-1}

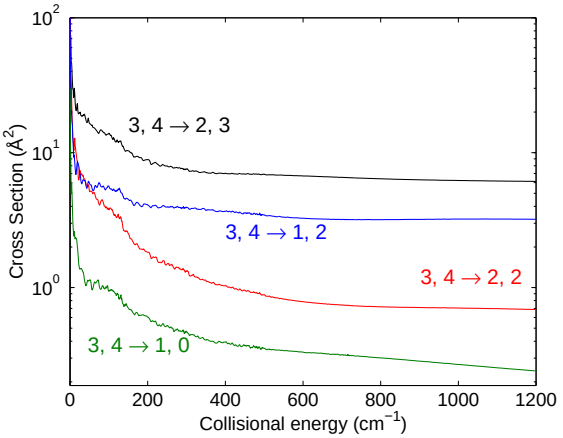

FIG. 6.— Collisional excitation cross sections of OH^+ by He out of $N, j = 3, 4$ state. (a) $\Delta j = \Delta N$ transitions. (b) $\Delta j \neq \Delta N$ transitions.

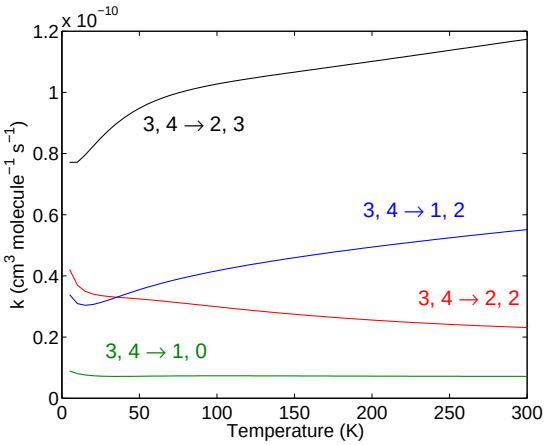

FIG. 7.— Temperature dependence of OH^+–He rate constants out of $N, J = 3, 4$ state.

In this section, we consider the collisional excitation of OH^+ by He. Helium, as a closed shell atom with two electrons, is sometimes considered as a reasonable template of molecular Hydrogen (Schöier et al. 2005; Lique et al. 2008). However, for a molecular cation such as OH^+, such approximation is expected to be moderately accurate due to the fact that the interaction of He and H_2 with an ion significantly differs. Generally, He rate coefficients underestimate H_2 rate coefficients by a factor that can be up to an order of magnitude (Roueff & Lique 2013).

In addition, OH^+ can react with H_2 to form H_2O^+. Then, it is really quite uncertain to estimate H_2-rate constants from the He ones. Nevertheless, we expect that the present data will enable rough estimate of the collisional excitation process of OH^+ in the ISM that is crucial for modeling the abundance and excitation of the OH^+ molecule.

To the best of our knowledge, no collisional rate constants for the OH^+ molecule have been published before. Within the Born-Oppenheimer approximation, scattering cross sections and corresponding rate constants are obtained by solving the motion of the nuclei on an electronic PES, which is independent of the masses and spins of the nuclei.

A new PES for OH^+ + He system has been calculated in this work as described in Appendix C. The average of the three-dimensional PES over the ground vibrational state of the OH^+ cation is shown in Figure 5. This two-dimensional effective potential is the one used in subsequent scattering calculations, described in Appendix D.

We have obtained the (de-)excitation cross sections for the first 19 fine structure levels of OH^+ by He. Figure 6 presents the typical kinetic energy variation of the integral cross sections for transitions from the fine structure level $(N, J) = (3, 4)$ of OH^+. There are noticeable resonances appearing at low and intermediate collisional energies. This is related to the presence of an attractive potential well, which allows for the He atom to be temporarily trapped there and hence quasi-bound states to be formed before the complex dissociates (Smith et al. 1979; Christoffel & Bowman 1983).

By performing a thermal average of the collision energy dependent cross sections obtained for the first 19 fine-structure OH^+ levels, we obtain rate constants for temperatures up to 300 K. The thermal dependence of the state-to-state OH^+–He rate constants is illustrated in Fig. 7 for transitions out of the $N, J = 3, 4$ level.

The rate constants shown in Fig. 7 exhibit interesting features that have important consequences on the magnitude of fine-structure-resolved rate constants:

(i) The rate constants decrease with increasing ΔN, which is the usual trend for rotational excitation. In addition, odd ΔN transitions are favored over even ΔN transitions. This is a consequence of the strong anisotropy of the PES.

(ii) A strong propensity rule exists for $\Delta J = \Delta N$ transitions.

Such $\Delta J = \Delta N$ propensity rule was predicted theoretically (Alexander & Dagdigian 1983) and is general for molecules in the $^3\Sigma^-$ electronic state. It was also observed previously for the $O_2(X^3\Sigma^-)$-He (Lique 2010), $SO(X^3\Sigma^-)$–He (Lique et al. 2005) or $NH(X^3\Sigma^-)$–He (Toboła et al. 2011; Dumouchel et al. 2012) collisions.

Then, we have calculated the hyperfine resolved OH^+–He rate coefficients using the procedure described in Appendix D. The complete set of de-excitation rate coefficients is available online from the BASECOL website (Dubernet, M.-L. et al.

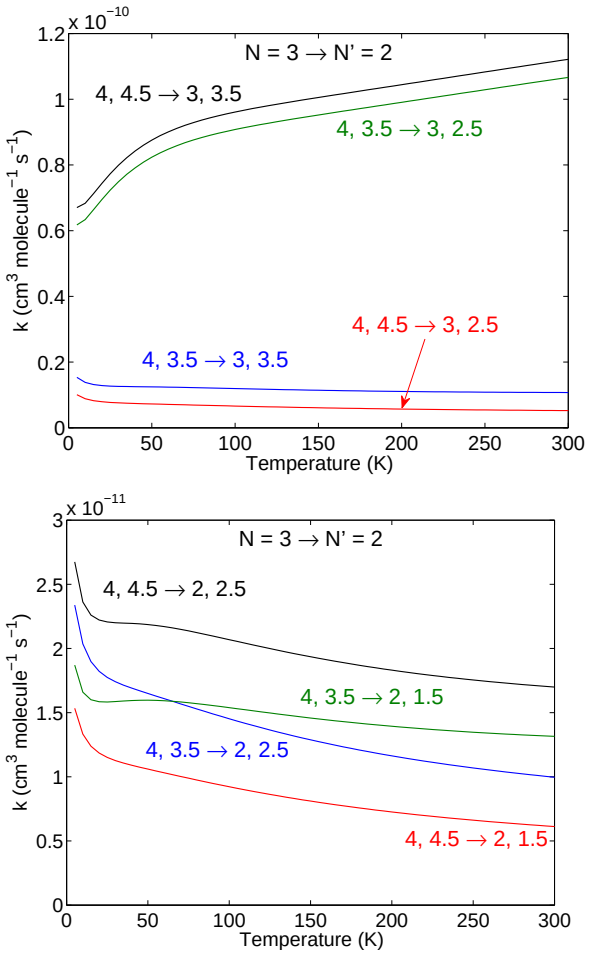

FIG. 8.— Temperature variation of the hyperfine resolved OH^+–He rate constants for $N = 3, J = 4, F \rightarrow N' = 2, J', F'$ transitions. Upper Panel: $\Delta J = \Delta N$ transitions. Lower Panel $\Delta J \neq \Delta N$ transitions. The numbers correspond to the $J, F \rightarrow J', F$ quantum numbers.

2013). Figure 8 presents the temperature variation of the OH^+–He rate constants for selected $N = 3, J, F \rightarrow N' = 2, J', F'$ transitions.

We have to distinguish $\Delta J = \Delta N$ and $\Delta J \neq \Delta N$ transitions in order to discuss the hyperfine propensity rules. For $\Delta J = \Delta N$ transitions, we have a strong propensity rule in favor of $\Delta J = \Delta F$ transitions, the propensity rule is also more pronounced when the N quantum number increases. This trend is the usual trend for open-shell molecules (Alexander 1985; Lique & Kłos 2011). For $\Delta J \neq \Delta N$ transitions, it is very difficult to find a clear propensity rules as already found for the CN molecule (Lique & Kłos 2011).

5. APPLICATIONS TO ASTRONOMICAL SOURCES

The computations performed in the previous sections provide an exhaustive dataset of the excitation processes of OH^+ that may strongly influence the modeling of astronomical sources. Such data are indeed critical to understand the physical conditions of regions where OH^+ is observed in emission, such as hot and dense PDRs (e.g. the Orion Bar, van der Tak et al. 2013), planetary nebulae (Etxaluze et al. 2014; Aleman et al. 2014) and the nuclei of active galaxies (van der Werf et al. 2010).

In these environments, van der Tak et al. (2013) proposed that the formation of OH^+ via

$$O^+ + H_2 \rightarrow OH^+ + H \quad (\Delta H_0 = -0.47 \text{ eV}) \qquad (4)$$

is sufficiently rapid to compete with (or even dominate) the non-reactive inelastic collisions in the excitation of the rotational levels of OH^+. Because of lack of information, they assumed that the probability of forming OH^+ in an excited level follows a Boltzmann distribution at a formation temperature $T_f = 2000$ K, i.e. $\sim$ one third of the exothermicity of the above reaction.

We break here from this approach and treat the chemistry and excitation of OH^+ self consistently in the framework of the Meudon PDR chemical model (Le Petit et al. 2006; Le Bourlot et al. 2012) in order to address the following questions. What are the relative importances of each process in the excitation of the rotational lines of OH^+ ? In particular, does the state-to-state rate constants substantially influence the emissivities of this species ?

5.1. *Modeling of hot and dense PDRs*

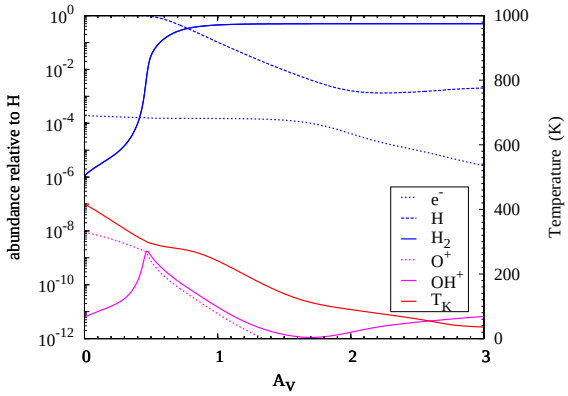

FIG. 9.— Kinetic temperature and abundances relative to total Hydrogen density of H, H_2, O^+, OH^+, and e^- computed with the Meudon PDR code as functions of the visual extinction from the ionization front across a prototypical hot and dense PDR (χ =10^4 and n=10^4 cm^{-3}).

We consider a prototypical hot and dense PDR, i.e. a one-dimensional slab of gas of total visual extinction $A_{V,\max} = 10$, with a density $n_H = 10^4$ cm^{-3}, a cosmic ray ionization rate $\zeta = 3 \times 10^{-16}$ s^{-1} (Indriolo et al. 2007; Indriolo & McCall 2012) and illuminated from one side by a UV radiation field of 10^4 that of the local ISRF (Mathis et al. 1983). The Meudon PDR code has been run using the standard chemical network available online (`http://pdr.obspm.fr/PDRcode.html`). The resulting kinetic temperature of the gas, its electronic fraction, and the relative abundances of H, H_2, O^+, and OH^+ are shown in Fig. 9 as functions of the distance from the ionization front. These chemical profiles indicate that the abundance of OH^+ peaks ($n(OH^+) \sim 1.8 \times 10^{-5}$ cm^{-3}) at $0.3 \leqslant A_V \leqslant 0.7$, i.e. in a region where the kinetic temperature $\sim$ 300 K, $n(e^-) \sim 1.6$ cm^{-3}, $n(\text{He}) \sim 10^3$ cm^{-3}, $n(O^+) \sim 1.3 \times 10^{-5}$ cm^{-3}, and where most of the Hydrogen is in atomic form ($n(H_2) = 10^2$ cm^{-3}).

The non reactive inelastic collision rates of OH^+ with H, H_2, He and e^- have all been implemented in the Meudon PDR code. For collisions with He we adopt the rates computed in the previous sections. For collisions with H and H_2,

we scale the OH^+-He collisional rates by using the cross sections calculated for He but using the good the reduced mass in the thermal average done to calculate the corresponding rate constants. At last for collisions with electrons we adopt the rates of van der Tak et al. (2013) given in their Appendix A and available on the LAMBDA website (Schöier et al. 2005) who performed detailed calculations of the $\Delta N = 1$ transitions. Given the large dipole moment of OH^+ we finally assume $k(\Delta N = 2) = 0.1 \times k(\Delta N = 1)$ and $k(\Delta N > 2) = 0$ (Faure & Tennyson 2001) for higher transitions of the OH^+-e^- system.

Concerning the chemical de-excitations, the destruction rates of $OH^+(N, J)$ are supposed to be independent from N, J for all the reactions involved in the destruction of OH^+. Inversely, we assume that the probabilities of forming OH^+ in an excited level follow a Boltzmann distribution at the kinetic temperature of the gas for all the reactions involved in the production of OH^+, except for reaction 4 for which we use our quantum calculations of the state-to-state rate constants.

5.2. *Intensities of the first rotational lines of OH^+*

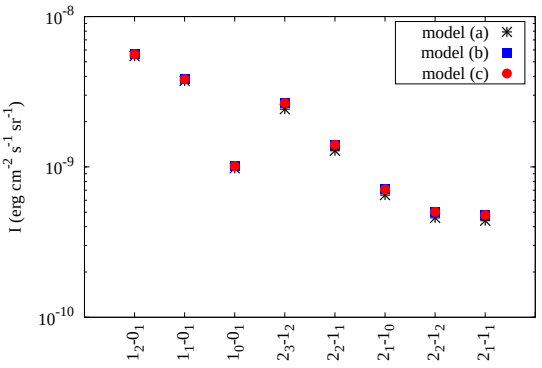

FIG. 10.— Continuum-subtracted intensities of the first rotational lines of OH^+ computed with the Meudon PDR code in the direction perpendicular to the slab for the models (a), (b), and (c) (see main text). Each $N'_{J'} - N''_{J''}$ line is labeled on the x-axis.

Following Zanchet et al. (2013b), the Meudon PDR code has been run in three different configurations: (a) considering only the excitation by nonreactive collisions, (b) including chemical pumping assuming that the probability to form OH^+ in an excited level via reaction 4 follows a Boltzmann distribution at a formation temperature of 2000 K (as done by van der Tak et al. 2013), and (c) adopting the branching ratios obtained with our quantum calculations (Table 3). The continumm-subtracted intensities in the direction perpendicular to the slab of the $N = 1 \rightarrow 0$ and $N = 2 \rightarrow 1$ rotational lines of OH^+ are shown in Fig. 10.

The analysis of the main excitation and de-excitation pathways at the peak of OH^+ abundance shows that the excitation of the $N < 3$ levels is primarily driven by inelastic collisions with electrons and atomic Hydrogen. As a result, the intensities of the $N = 1 - 0$ and $N = 2 - 1$ transitions predicted by models with density ranging between 10^4 and 10^5 cm^{-3} increase by less than 10% when we take the chemical pumping into account. Moreover we find no substantial difference between the models computed with detailed state-to-state chemical rates and those obtained with a Boltzmann distribution function. The chemical pumping has a stronger impact on the population of the $N > 2$ levels, but only in the inner parts of the cloud where the kinetic temperature is lower.

While these results stress the importance of detailed calculations of inelastic collisional rates, they do not preclude the existence of interstellar media where the integrated intensities of the rotational lines of OH^+ may be driven by chemical pumping. Indeed the abundance of OH^+ peaks in a region of the cloud where the abundance of H_2 varies over more than four orders of magnitude (see Fig. 9). A slightly broader peak of OH^+ that extends towards the molecular region, as it is the case in media with constant thermal pressure rather than constant density (van der Tak et al. 2013), would thus greatly enhance the influence of chemical pumping through reaction 4. To study these effects, we will perform a more complete analysis of different astrophysical environments in a forthcoming paper. This will be done in the framework of both the Meudon PDR code and the MADEX radiative transfer model (Cernicharo 2012) in order to also address the impact of the fluorescence on the excitation of the OH^+ rotational lines.

6. CONCLUSIONS

In this work the state-to-state rate constants for the formation of $OH^+(X^3\Sigma^-)$ products in the reaction O^++$H_2(J = 0, 1)$ have been obtained using an accurate quantum wave packet treatment, on the ground electronic state of the system. In these calculations the electronic spin is not account for, so that it is assumed that the rate to form $F_1(J = N+1)$, $F_2(J = N)$ and $F_3(J = N-1)$ sublevels are the same to that of a given final N value obtained here. The results obtained have been fitted to an analytical form in the (0,5000)K temperature interval, and the parameters thus obtained are listed in the Appendix.

The state-to-state Einstein coefficient for the $^3\Sigma^-$ - $^3\Sigma^-$, $^3\Sigma^-$ - $^3\Pi$ and $^3\Pi$ - $^3\Pi$ bands have been calculated and provided in the Appendix. For that purpose very accurate potential energy curves of several electronic states of OH^+ have been calculated, and their corresponding transition dipole moment. The empirical spin-orbit, spin-rotation and spin-spin constants have been used (Merer et al. 1975; Gruebele et al. 1986). The rovibrational state on each electronic state have been calculated and the radial dipole moments have been calculated numerically. These results are intended to be included in astrophysical PDR model to account for the IR and UV radiative transfer due to the radiation flux. The radiative lifetimes obtained here, of $\approx$ 2500 ns, are in good agreement with the experimental results of Möhlmann et al. (1978), and 2.5 times longer than the values reported by Brzozowski et al. (1974) which were used by de Almeida & Singh (1981) to get semi-empirical Eisntein's coefficients.

Also collisional OH($X^3\Sigma^-$) + He inelastic rates have been obtained, including hyperfine structure and using a new potential energy surface. These are used in the astrophysical model used here and also to extrapolate the corresponding rates for OH($X^3\Sigma^-$) + H and OH($X^3\Sigma^-$) + H_2.

All the rates computed in this work have been used in astrophysical models of highly illuminated isochoric photodissociation regions. These models show that OH^+ is formed in regions where the kinetic temperature is high and the density of H_2 is low. Under such conditions, we find that chemical pumping does not play a significant role (about 10% or less) on the excitation of OH^+ whose rotational levels are mainly populated through inelastic collisions. We propose that chemical pumping may be more efficient if OH^+ was formed in regions with larger molecular fraction (such as isobaric PDRs)

but this has yet to be confirmed with additional modeling. Given the importance of inelastic collisions, additional computations are now in progress in order to derive more reliable estimates of the collisional rates between $OH^+(^3\Sigma^-)$ and both H and H_2.

7. ACKNOWLEDGMENTS

This work has been supported by the of Ministerio de Economía e Innovación under grants CSD2009-00038, FIS2011-29596-C02 and CTQ2012-37404-C02. NB acknowledges the Scientific and Technological Council of Turkey for TR-Grid facilities (TUBITAK; Project No. TBAG-112T827). ME, JRG and JC thank the Spanish MINECO for funding support from grants AYA2009-07304 and AYA2012-32032. OR, AA and NB also acknowledge CSIC for a travelling grant I-LINK0775. We acknowledge the CNRS national program "Physique et Chimie du Milieu Interstellaire" for supporting this research. F.L. acknowledge support by the Agence Nationale de la Recherche (ANR-HYDRIDES), contract ANR-12-BS05-0011-01. J.K. acknowledges the U. S. National Science Foundation (grant CHE-1213322 to Prof. M. H. Alexander). The calculations have been perfomed in the parallel facilities at CESGA computing center, through ICTS grants, which are acknowledged.

8. APPENDIX A: STATE-TO-STATE REACTION RATE CONSTANTS

The state-to-state reaction rate constants are computed with a time dependent WP method, using a modified Chebyshev integrator (Huang et al. 1994; Mandelshtam & Taylor 1995; Huang et al. 1996; Kroes & Neuhauser 1996; Chen & Guo 1996; Gray & Balint-Kurti 1998; González-Lezana et al. 2005). The WP is represented in reactant Jacobi coordinates in a body-fixed frame, which allows to account for the permutation symmetry of H_2. At each iteration, a transformation to products Jacobi coordinates is performed in order to analyze the final flux on different $OH^+(v', N)$ channels, using the method described by Gómez-Carrasco & Roncero (2006). The calculation are performed using the MAD-WAVE3 program (Zanchet et al. 2009). The parameters used in the propagation are listed in Table 2.

TABLE 2
Parameters used in the wave packet calculations in reactant Jacobi coordinates. The function used for the absoprtion has the form $f(X) = \exp\left[-A_X\left(\frac{X-X_{abs}}{b}\right)^n\right]$ for $X > X_{abs}$ and $f(X) = 1$ elsewhere, with $X \equiv R$ and r, with $n = 4$ and $b = 2$. Distances are in Å and energies in eV.

r_{min}, r_{max}, N_r	0.2, 30, 256
r_{abs}, A_r	16, 3 10^{-6}
R_{min}, R_{max}, N_R	0.32, 36, 620
R_{abs}, A_R	16 , 10^{-6}
N_γ	160 in $[0, \pi/2]$
R_0 , E_0 , ΔE	13, 0.2, .1
R'_∞	11
V_{cut}	3.7
E^ℓ_{cut}	5
Ω_{max}	7
Ω'_{max}	25

In order to get convergence at collisional energies of ≈ 1 meV, the absorption parameters have been fitted carefully to avoid the reflection of the WP. Also, to get convergence at so low energy, a large number Chebyshev iterations have been performed. This number decreases as total angular momentum, J_t, increases, because the centrifugal barrier shifts the energy threshold towards higher energies and increases the resonances' widths. More than 100000 iterations were used for $J_t < 10$, about 50000 in the interval $10 < J_t < 20$, and 30000 or less for $J_t > 20$. The total reaction probabilities in the low collision energy range for some selected J_t values are compared in Fig. 11 with time-independent (TI) calculations performed using a coupled channel hyperspherical coordinate method as implemented in the ABC code (Skouteris et al. 2000). The comparison shows an excellent agreement down to collision energies lower than 1 meV.

The reaction is exothermic and rather fast and, therefore, the Coriolis couplings do not mix too many helicity states, characterized by the projection of the total angular momentum $\mathbf{J}_t$ on the z-axis of the body-fixed frame, Ω. As found earlier for this system (Martínez et al. 2006; Xu et al. 2012), a maximum value of $\Omega_{max} = 7$ is enough to get good convergence. At each iteration the wave packet is transformed from the reactants to the products body-fixed frame, and in the products frame a maximum number of Ω'_{max} = 24 is used. In order to control the reactant to product transformation of coordinates, the sum of all the individual state-to-state reaction probabilities (shown in Fig. 11) is compared with that obtained by the flux method (Miller 1974; Zhang & Zhang 1994; Neuhauser 1994; Goldfield et al. 1995). In all cases, the agreement is better than 1%.

The reaction probabilities have been calculated for all J_t up to $J_t = 30$. After this value, only partial waves for J_t in multiple of 5 have been calculated up to J_t=80 and for all initial he-

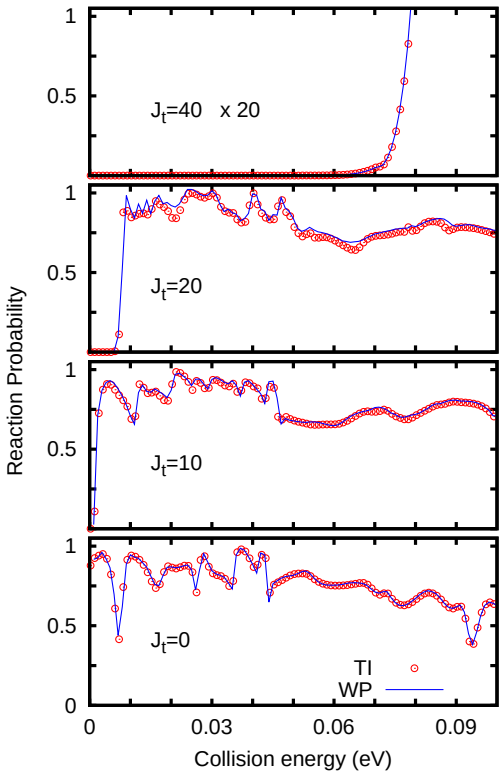

FIG. 11.— Reaction probabilities for the O^++$H_2(v = 0, J = 0, J_t)$, for different J_t values as a function of collision energy. Blue lines are the wave packet results obtained with MADWAVE3 code. Open red circles are the time-independent results obtained with the ABC TI scattering code.

licities $\Omega_0 = 0, ..., min(J, J_t)$ and the two parity under inversion of spatial coordinates. For the non-calculated intermediate J_t values, the reaction probabilities are obtained using a J-shifting based interpolation, as used before by Aslan et al. (2012); Zanchet et al. (2013b). The convergence of this approach has been tested by comparing the total integral reaction cross section with that using less number of J_t values, giving an agreement better than 2%.

The state-to-state rate constants of the $H_2(v = 0, J = 0, 1)$+ $O^+ \rightarrow$ H + $OH^+(v', N)$ reactive collisions have been fitted in the 50-5000 K temperature range to the expression

$$k_{v',N}(T) = cT^b \exp(d/T - aT) \quad 10^{-9}\mathrm{cm}^3/\mathrm{s}$$

where T is in Kelvin. The parameters a, b, c, and d depend on the initial $H_2(v, J)$ and final $OH^+(v', N)$ states and are listed in table 3.

TABLE 3
Parameters used to fit the state-to-state rate constants, according to Eq. (5), for $O^+ + H_2(v, J) \rightarrow H + OH^+(v', N)$.

N	c	b	a × 1000	d
$O^+ + H_2(v = 0, J = 0) \rightarrow H + OH^+(v' = 0, N)$				
0	0.2642E-01	0.1125	0.2543	-128.6513
1	0.7329E-01	0.0847	0.2407	-105.5280
2	0.1144E+00	0.0295	0.2014	-66.0416
3	0.2001E+00	-0.0588	0.1426	-47.4437
4	0.2352E+00	-0.0807	0.1234	-40.9251
5	0.2764E+00	-0.1180	0.1104	-28.9175
6	0.5798E+00	-0.2418	0.0659	-27.7198
7	0.5885E+00	-0.2520	0.0592	-24.1934
8	0.4493E+00	-0.2222	0.0668	-23.3146
9	0.4858E+00	-0.2387	0.0708	-29.2944
10	0.3966E+00	-0.2170	0.0711	-28.6389
11	0.2131E+00	-0.1421	0.0807	-33.7970
12	0.1478E+00	-0.1126	0.0799	-37.3616
13	0.5621E-01	-0.0247	0.0748	-22.3201
14	0.3229E-01	0.0140	0.0685	-32.7974
15	0.2872E-02	0.2924	0.1120	-67.0153
16	0.4806E-06	1.4175	0.3711	-0.0028
17	0.1200E-08	2.1348	0.4843	-0.0027
18	0.5969E-11	2.7550	0.5812	-0.0028
19	0.7767E-13	3.2592	0.6782	-0.0032
20	0.1965E-15	3.6601	0.7370	-0.0032
21	0.3068E-16	4.1274	0.8156	-0.0035
22	0.1796E-17	4.3997	0.8392	-0.0034
$O^+ + H_2(v = 0, J = 0) \rightarrow H + OH^+(v' = 1, N)$				
0	0.7654E-01	-0.1131	0.1579	-93.1416
1	0.6630E-01	0.0100	0.1786	-52.6948
2	0.6690E-01	-0.0015	0.1414	-33.0402
3	0.2440E+00	-0.1824	0.0821	-49.1025
4	0.3277E+00	-0.2307	0.0562	-36.2931
5	0.3474E+00	-0.2639	0.0220	-24.5429
6	0.5062E+00	-0.3307	0.0050	-31.8403
7	0.1592E+00	-0.1843	0.0516	-143.9353
8	0.8583E-01	-0.1036	0.0914	-518.6398
9	0.1506E+00	-0.2041	0.0690	-908.0244
10	0.6036E-06	1.4279	0.4508	-0.0039
11	0.1361E-07	1.8738	0.4999	-0.0028
12	0.5250E-09	2.2663	0.5603	-0.0029
13	0.2768E-10	2.6122	0.6105	-0.0030
14	0.1386E-11	2.9556	0.6522	-0.0030
15	0.2221E-12	3.1393	0.6501	-0.0029
16	5.0251E-18	4.5027	0.8880	-0.0001
17	3.2730E-18	4.5027	0.8880	-0.0001
18	0.2130E-17	4.5027	0.8801	-0.0036
19	0.1380E-18	4.7881	0.9153	-0.0037
20	0.5397E-18	4.4867	0.7874	-0.0033

9. APPENDIX B: OH^+ EINSTEIN COEFFICIENTES

In order to incorporate electronic transitions in the radiative models, we have calculated seven potential energy curves of the OH^+ cation, correlating with the $O(^3P)$+H^+, $O^+(^4S)$+$H(^2S)$ and $O(^1D)$+H^+ dissociation channels, using the MOLPRO package (MOLPRO 2010) for *ab initio* electronic calculations. The calculations initially consisted of a full valence state-averaged complete active space procedure (SA-CASSCF) including all the molecular orbitals arising from the valence atomic orbitals (8 electrons in 5 orbitals). The C_{2v} point group of symmetry has been used. The state-averaged electronic wavefunction included all the states correlating with the above-mentioned asymptotes, two $^3\Sigma^-$, one $^3\Pi$, one $^1\Sigma^+$, one $^1\Delta$, one $^1\Pi$ and one $^5\Sigma^-$ electronic states. These number of states ensures the correct degeneracy

$O^+ + H_2(v=0,J=1) \rightarrow H + OH^+(v'=0,N)$				
0	0.4216E-02	0.2224	0.2236	-23.2949
1	0.1089E-01	0.2557	0.2377	-19.5720
2	0.2190E-01	0.2270	0.2318	-20.3101
3	0.6200E-01	0.1099	0.1939	-25.9693
4	0.1882E+00	-0.0349	0.1377	-34.3086
5	0.3235E+00	-0.1204	0.0931	-35.2714
6	0.3053E+00	-0.1404	0.0726	-24.7791
7	0.4544E+00	-0.2133	0.0572	-24.0813
8	0.3988E+00	-0.2134	0.0564	-24.4975
9	0.2089E+00	-0.1394	0.0831	-19.5044
10	0.2260E+00	-0.1534	0.0885	-28.3408
11	0.1936E+00	-0.1428	0.0796	-28.4596
12	0.6348E-01	-0.0158	0.0944	-17.7454
13	0.2635E-01	0.0671	0.1025	-18.2581
14	0.1827E-01	0.0649	0.0788	-29.9789
15	0.1409E-02	0.3549	0.1156	-20.4638
16	0.8814E-06	1.3023	0.3317	-0.0026
17	0.5001E-08	1.9172	0.4424	-0.0025
18	0.1706E-10	2.6009	0.5720	-0.0030
19	0.1556E-12	3.1589	0.6664	-0.0032
20	0.3814E-06	0.9388	-0.0935	-0.0009
21	0.9051E-16	3.9766	0.8019	-0.0034
22	0.8370E-17	4.1892	0.8050	-0.0033
$O^+ + H_2(v=0,J=1) \rightarrow H + OH^+(v'=1,N)$				
0	0.3753E-01	-0.1096	0.1175	-126.3446
1	0.1323E+00	-0.1232	0.1292	-153.8032
2	0.4300E-01	0.0738	0.1825	-59.5045
3	0.6226E-01	0.0309	0.1558	-32.2931
4	0.4331E+00	-0.2623	0.0362	-42.6035
5	0.3119E+00	-0.2377	0.0372	-33.0488
6	0.3304E+00	-0.2614	0.0324	-20.8766
7	0.3757E+00	-0.3033	0.0213	-39.8215
8	0.2547E+00	-0.2644	0.0405	-352.3149
9	0.2390E-02	0.3403	0.1918	-373.4869
10	0.7570E-05	1.0464	0.2998	-0.0017
11	0.8401E-07	1.6516	0.4783	-0.0029
12	0.1604E-08	2.1177	0.5401	-0.0029
13	0.9677E-10	2.4569	0.5985	-0.0029
14	0.4207E-11	2.8035	0.6315	-0.0029
15	0.3221E-18	4.3612	1.0000	-0.0010
16	0.2129E-18	4.3612	1.0002	-0.0010
17	0.1392E-17	4.3600	1.0001	-0.0010
18	0.5176E-17	4.3612	0.8616	-0.0036
19	0.3496E-18	4.6391	0.8928	-0.0036
20	0.1317E-15	3.6978	0.5835	-0.0028

of the states at the dissociation limits. These wavefunctions were used as reference for a subsequent internally contracted multireference configuration interaction (icMRCI) calculation, where all single and double excitations were included. Finally, the Davidson correction (+Q) (Davidson 1975) was applied to the final energies in order to approximately account for the contribution of higher excitations. Calculations have been performed with three correlation-consistent polarized basis set of Dunning, denoted aug-cc-pVnZ (n = Q, 5 and 6), and the extrapolation to complete basis set (CBS, $n=\infty$) has been also obtained using the following extrapolation formula (D. E. Woon and Jr. T. H. Dunning 1994):

$$E(n) = E_{CBS} + Be^{-(n-1)} + Ce^{-(n-1)^2}.$$

The CBS electronic energy curves are displayed in the top panel of Fig. 4.

In order to calculate the ro-vibrational states of OH^+, we use the effective Hamiltonian (Lefebvre-Brion & Field 1986)

$$H = -\frac{\hbar^2}{2\mu}\frac{1}{R^2}\frac{\partial}{\partial R}R^2\frac{\partial}{\partial R} + \frac{\mathbf{R}^2}{2\mu R^2} + \frac{2}{3}\lambda\left(3\mathbf{S}_z^2 - \mathbf{S}^2\right) + \gamma\mathbf{R}\cdot\mathbf{S} + V, \quad (5)$$

where the third and forth terms are the spin-spin and the spin-rotation terms. In this equation V is the *ab initio* potential energy curves calculated for the $X^3\Sigma^-$ and $A^3\Pi$ states. The spin-orbit is included as an empirical parameter taken from Merer et al. (1975). The $X^3\Sigma^-$ state is represented in the Hund's case (b), with the parameters γ= -0.15126 cm^{-1} and $\lambda = 2.1429$ cm^{-1} as determined in measurements of the rotational spectra (Gruebele et al. 1986). The $A^3\Pi$ states are represented in the Hund's case (a), with $\gamma = 0.01730$ cm^{-1} taken from Merer et al. (1975).

The total wavefunction of OH^+ is factorized as

$$\Psi_{\alpha,v}^{JM;S\Lambda} = \frac{\Phi_v^{JS\Lambda;\alpha}(R)}{R}\left|JMS\Lambda;\alpha\right\rangle, \quad (6)$$

where the quantum number $\alpha = N$ for Hund's case (b) to describe $X^3\Sigma^-$, while $\alpha = \Sigma$ or $\Omega = \Lambda + \Sigma$ for Hund's case (a) for $A^3\Pi$.

The radial functions in Eq. (6) are the numerical solutions of the one-dimensional Schrödinger equation

$$\left\{-\frac{\hbar^2}{2\mu}\frac{d^2}{dR^2} + \hbar^2\frac{C}{2\mu R^2} + V(R) - E_v^{JS\Lambda\alpha}\right\}\varphi_v^{JS\Lambda;\alpha}(R) = 0. \quad (7)$$

with

$$C = \begin{cases} N(N+1) - \Lambda^2 & \text{for } {}^3\Sigma^- \quad \text{case (b)} \\ J(J+1) - \Omega^2 + S(S+1) - \Sigma^2 & \text{for } {}^3\Pi \quad \text{case (a)} \end{cases}$$

The rovibrational states have been obtained numerically, in a grid of 12000 points in the $(0.4, 14)$ a.u. interval. Vibrational levels up to $v = 20$ and $v = 12$ have been considered for X and A states, respectively. The higher rotational level considered are $N = 35$, for ${}^3\Sigma^-$, and $J = 35$ for ${}^3\Pi_\Omega$.

In Hund's case (b), the angular functions in Eq. (6) are defined as

$$\left|JMS\Lambda;N\right\rangle = \sum_{M_S,M_N}(-1)^{S-N+M}\sqrt{2J+1}\begin{pmatrix} S & N & J \\ M_S & M_N & M\end{pmatrix} \times \left|SM_S\right\rangle\left|NM_N\Lambda\right\rangle \quad (8)$$

where M, M_S and M_N are the projections of $\mathbf{J}$, $\mathbf{S}$ and $\mathbf{N}$ angular momenta, respectively, on the z-axis of the laboratory frame. $|SM_S\rangle$ are the spin functions and

$$\left|NM_N\Lambda\right\rangle = \sqrt{\frac{2N+1}{4\pi}}D_{M_N\Lambda}^{N*}(\phi,\theta,0)\left|\Lambda\right\rangle \quad (9)$$

where $D_{M_N\Lambda}^{N*}$ are Wigner rotation matrices (Zare 1988) and Λ is the projection of the electronic orbital angular momentum on the internuclear axis, used to label the electronic state $|\Lambda\rangle$.

In Hund's case (a) the angular functions are

$$\left|JMS\Lambda;\Sigma\right\rangle = \sqrt{\frac{2J+1}{4\pi}}D_{M\Omega}^{J*}(\phi,\theta,0)\left|\Lambda\right\rangle\left|S,\Sigma\right\rangle, \quad (10)$$

where Σ is the projections of the electronic spin on the internuclear axis, and $\Omega = \Lambda + \Sigma$.

The transformation between the two angular basis sets is given by

$$|JMS\Lambda;N\rangle = \sum_{\Sigma}(-1)^{S-N+\Omega}\sqrt{2N+1}\begin{pmatrix} S & N & J \\ \Sigma & \Lambda & -\Omega \end{pmatrix} |JMS\Lambda;\Sigma\rangle \quad (11)$$

The total energy, considering spin-spin and spin-rotation terms in the Hamiltonian, for the $^3\Sigma^-$ states in the b Hund's case are given by (Herzberg 1950)

$$\begin{aligned} F_1 &= E_v^{JS\Lambda N} - \frac{2}{3}\lambda\frac{N}{2N+3} + \gamma N \quad \text{with} \quad J = N+1 \\ F_2 &= E_v^{JS\Lambda N} + \frac{2}{3}\lambda - \gamma \quad \text{with} \quad J = N \\ F_3 &= E_v^{JS\Lambda N} - \frac{2}{3}\lambda\frac{N+1}{2N-1} - \gamma(N+1) \quad \text{with} \quad J = N-1 \end{aligned} \quad (12)$$

and for the $^3\Pi$ states in the Hund's case a are given by

$$\begin{aligned} F_3 &= E_v^{JS\Lambda\Sigma=-1} - \gamma + \Delta T_0 \quad \text{with} \quad \Omega = 0 \\ F_2 &= E_v^{JS\Lambda\Sigma=0} - 2\gamma + \Delta T_1 \quad \text{with} \quad \Omega = 1 \\ F_1 &= E_v^{JS\Lambda\Sigma=1} - \gamma + \Delta T_2 \quad \text{with} \quad \Omega = 2. \end{aligned} \quad (13)$$

with ΔT_Ω = 0, 83 and 167 cm^{-1}, for $\Omega = 0, 1$ and 2, respectively, associated to the empirical spin-orbit splittings (Merer et al. 1975). These three states are doubly degenerate, $g = 2$, and in the case of $\Omega = 0$ we do consider the 0^+ and 0^- states as degenerate.

The Einstein coefficients are given by

$$A^{\Lambda S\Sigma;\Lambda' S'\Sigma'}_{Jv;J'v'} = \frac{1}{3\pi\epsilon_0\hbar^4}\left(\frac{h\nu}{c}\right)^3 \delta_{SS'}\left|M^{J\Lambda S\alpha;J'\Lambda' S'\alpha'}_{v;v'}\right|^2 \times \frac{S^{J\Lambda S;J'\Lambda' S'}_{\alpha\alpha'}}{2J+1}, \quad (14)$$

where the radial integrals are given by

$$M^{J\Lambda S\alpha;J'\Lambda' S'\alpha'}_{v;v'} = \int dR\, \Phi_v^{J\Lambda S\alpha *}(R)\,\langle\Lambda|d_q|\Lambda'\rangle\,\Phi_{v'}^{J'\Lambda' S'\alpha'}(R),$$

and are perfomed numerically using $\langle\Lambda|d_q|\Lambda'\rangle$ values calculated with the MOLPRO package. The $M^{J\Lambda S\alpha;J'\Lambda' S'\alpha'}_{v;v'}$ matrix elements obtained in this work are also listed for different electronic transitions, $X^3\Sigma^- \leftarrow X^3\Sigma^-$, $A^3\Pi_\Omega \leftarrow A^3\Pi_\Omega$ and $A^3\Pi_\Omega \leftarrow X^3\Sigma^-$, in the tables listed below.

The Hönl-London factors in Eq. (14) depend on the Hund's case used, and becomes:

$$S^{J\Lambda S;J'\Lambda' S'}_{\alpha\alpha'} = \frac{(2J+1)(2J'+1)(2N+1)(2N'+1)}{3} \times \begin{pmatrix} N & 1 & N' \\ -\Lambda & q & \Lambda' \end{pmatrix}^2 \begin{Bmatrix} J & N & S \\ N' & J' & 1 \end{Bmatrix}^2 \quad (15)$$

for $^3\Sigma(b) \leftarrow^3 \Sigma(b)$ transitions,

$$S^{J\Lambda S;J'\Lambda' S'}_{\alpha\alpha'} = \frac{(2J+1)(2J'+1)}{3}\begin{pmatrix} J & 1 & J' \\ \Omega & q & -\Omega' \end{pmatrix}^2 \quad (16)$$

for $^3\Pi(a) \leftarrow^3 \Pi(a)$, and

$$S^{J\Lambda S;J'\Lambda' S'}_{\alpha\alpha'} = \frac{(2J+1)(2J'+1)(2N+1)}{3} \times \begin{pmatrix} J & 1 & J' \\ \Lambda+\Sigma & q & -\Lambda'-\Sigma \end{pmatrix}^2 \begin{pmatrix} S & N & J \\ \Sigma & \Lambda & -\Lambda-\Sigma \end{pmatrix}^2 \quad (17)$$

for mixed $^3\Pi(a) \leftarrow^3 \Sigma(b)$ transitions.

In the tables below we report total energies and the electric dipole moments, $\left|M^{J\Lambda S\alpha;J'\Lambda' S'\alpha'}_{v;v'}\right|^2$ required to calculate the Einstein coefficients in Eq. (14) for different electronic transitions: $X^3\Sigma^- \leftarrow X^3\Sigma^-$, $A^3\Pi_\Omega \leftarrow A^3\Pi_\Omega$ and $A^3\Pi_\Omega \leftarrow X^3\Sigma^-$.

In order to reduce the length of the table, only those values for $\left|M^{J\Lambda S\alpha;J'\Lambda' S'\alpha'}_{v;v'}\right|^2 > 0.1$ (10^{-3} for $\Sigma - \Pi$ transitions) and since the dependence of $\left|M^{J\Lambda S\alpha;J'\Lambda' S'\alpha'}_{v;v'}\right|^2$ on the rotational quantum numbers $J\alpha; J'\alpha'$ is weak, we shall only list the matrix elements for the lower rotational transition which are larger than 10^{-3} for each electronic transition considered here. The Hönl-London factors, containing the main dependence of the Einstein coefficients on the rotational transitions, can be easily evaluated using the expressions of this appendix.

TABLE 4 $^3\Sigma^- - ^3\Sigma^-$ transition electric dipole matrix elements (in a.u.) for N_X=0, J_X=1, N'_X=1 , J'_X=0

v_X	E_{vNJ}(cm^{-1})	v'_X	$E_{v'N'J'}$(cm^{-1})	$\lvert M\rvert^2$ (a.u.)
0	1540.906	0	1571.238	0.832
0	1540.906	1	4528.533	0.005
1	4499.658	0	1571.238	0.005
1	4499.658	1	4528.533	0.911
1	4499.658	2	7329.110	0.010
2	7301.650	1	4528.533	0.011
2	7301.650	2	7329.110	0.997
2	7301.650	3	9979.210	0.016
3	9953.124	2	7329.110	0.018
3	9953.124	3	9979.210	1.091
3	9953.124	4	12484.909	0.022
4	12460.153	3	9979.210	0.025
4	12460.153	4	12484.909	1.193
4	12460.153	5	14852.246	0.029
5	14828.776	4	12484.909	0.032
5	14828.776	5	14852.246	1.303
5	14828.776	6	17087.175	0.036
5	14828.776	7	19195.549	0.001
6	17064.943	5	14852.246	0.040
6	17064.943	6	17087.175	1.422
6	17064.943	7	19195.549	0.043
6	17064.943	8	21183.090	0.002
7	19174.511	5	14852.246	0.001
7	19174.511	6	17087.175	0.048
7	19174.511	7	19195.549	1.549
7	19174.511	8	21183.090	0.051
7	19174.511	9	23055.314	0.003
8	21163.200	6	17087.175	0.002

$^3\Sigma^- - ^3\Sigma^-$ transitions (continuation)				
8	21163.200	7	19195.549	0.056
8	21163.200	8	21183.090	1.684
8	21163.200	9	23055.314	0.058
8	21163.200	10	24817.468	0.004
9	23036.530	7	19195.549	0.003
9	23036.530	8	21183.090	0.064
9	23036.530	9	23055.314	1.828
9	23036.530	10	24817.468	0.065
9	23036.530	11	26474.473	0.005
10	24799.750	8	21183.090	0.004
10	24799.750	9	23055.314	0.072
10	24799.750	10	24817.468	1.981
10	24799.750	11	26474.473	0.072
10	24799.750	12	28030.851	0.006
11	26457.784	9	23055.314	0.005
11	26457.784	10	24817.468	0.080
11	26457.784	11	26474.473	2.143
11	26457.784	12	28030.851	0.079
11	26457.784	13	29490.540	0.008
11	26457.784	14	30856.851	0.001
12	28015.158	10	24817.468	0.007
12	28015.158	11	26474.473	0.088
12	28015.158	12	28030.851	2.315
12	28015.158	13	29490.540	0.085
12	28015.158	14	30856.851	0.009
12	28015.158	15	32132.402	0.002
13	29475.813	11	26474.473	0.008
13	29475.813	12	28030.851	0.096
13	29475.813	13	29490.540	2.498
13	29475.813	14	30856.851	0.092
13	29475.813	15	32132.402	0.011
13	29475.813	16	33318.965	0.002
14	30843.067	11	26474.473	0.001
14	30843.067	12	28030.851	0.010
14	30843.067	13	29490.540	0.104
14	30843.067	14	30856.851	2.696
14	30843.067	15	32132.402	0.098
14	30843.067	16	33318.965	0.013
14	30843.067	17	34416.761	0.003
15	32119.545	12	28030.851	0.002
15	32119.545	13	29490.540	0.012
15	32119.545	14	30856.851	0.112
15	32119.545	15	32132.402	2.912
15	32119.545	16	33318.965	0.105
15	32119.545	17	34416.761	0.014
15	32119.545	18	35424.375	0.003
16	33307.025	13	29490.540	0.002
16	33307.025	14	30856.851	0.013
16	33307.025	15	32132.402	0.120
16	33307.025	16	33318.965	3.154
16	33307.025	17	34416.761	0.113
16	33307.025	18	35424.375	0.015
16	33307.025	19	36341.801	0.004
16	33307.025	20	37173.035	0.001

$^3\Sigma^- - ^3\Sigma^-$ transitions (continuation)				
17	34405.749	14	30856.851	0.003
17	34405.749	15	32132.402	0.015
17	34405.749	16	33318.965	0.130
17	34405.749	17	34416.761	3.438
17	34405.749	18	35424.375	0.124
17	34405.749	19	36341.801	0.016
17	34405.749	20	37173.035	0.006
18	35414.305	15	32132.402	0.004
18	35414.305	16	33318.965	0.016
18	35414.305	17	34416.761	0.143
18	35414.305	18	35424.375	3.791
18	35414.305	19	36341.801	0.141
18	35414.305	20	37173.035	0.016
19	36332.666	16	33318.965	0.005
19	36332.666	17	34416.761	0.017
19	36332.666	18	35424.375	0.163
19	36332.666	19	36341.801	4.234
19	36332.666	20	37173.035	0.165
20	37164.793	16	33318.965	0.001
20	37164.793	17	34416.761	0.006
20	37164.793	18	35424.375	0.017
20	37164.793	19	36341.801	0.191
20	37164.793	20	37173.035	4.775

TABLE 5 $^3\Pi_0 - ^3\Pi_0$ transition electric dipole matrix elements (in a.u.) for J_A=0, J'_A=1. The corresponding matrix elements for $^3\Pi_1 - ^3\Pi_1$ and $^3\Pi_2 - ^3\Pi_2$ transitions are nearly identical and are omitted for simplicity

v_A	E_{vJ}(cm^{-1})	v'_A	$E_{v'J'}$(cm^{-1})	$\|M\|^2$ (a.u.)
0	29590.117	0	29616.792	1.309
1	31568.468	1	31593.447	1.586
2	33389.971	2	33413.313	1.917
3	35060.018	3	35081.762	2.316
3	35060.018	4	36601.163	0.131
4	36581.006	3	35081.762	0.141
4	36581.006	4	36601.163	2.812
4	36581.006	5	37970.365	0.177
5	37951.821	4	36601.163	0.191
5	37951.821	5	37970.365	3.447
5	37951.821	6	39183.750	0.230
6	39166.901	5	37970.365	0.251
6	39166.901	6	39183.750	4.302
6	39166.901	7	40228.488	0.295
7	40213.525	6	39183.750	0.324
7	40213.525	7	40228.488	5.553
7	40213.525	8	41076.108	0.368
8	41063.494	7	40228.488	0.412
8	41063.494	8	41076.108	7.717
8	41063.494	9	41669.175	0.437
9	41659.736	8	41076.108	0.505
9	41659.736	9	41669.175	12.384

$^3\Pi_0 - ^3\Pi_0$ transitions (continuation)				
9	41659.736	10	42018.670	0.531
10	42011.891	9	41669.175	0.655
10	42011.891	10	42018.670	20.115
10	42011.891	12	42170.746	0.235
11	42145.175	10	42018.670	0.105
11	42145.175	11	42146.684	85.773
11	42145.175	12	42170.746	1.858
12	42168.395	10	42018.670	0.342
12	42168.395	11	42146.684	3.633
12	42168.395	12	42170.746	69.643

TABLE 6 $^3\Sigma^-$ - $^3\Pi_0$ transition electric dipole matrix elements (in a.u.) for N_x=0, J_X=1 and J'_A=0. The corresponding matrix elements for $^3\Sigma^-$ -$^3\Pi_1$ and $^3\Pi_2 - ^3\Pi_2$ transitions are nearly identical and are omitted for simplicity

v_X	E_{vNJ}(cm^{-1})	v'_A	$E_{v'J'}$(cm^{-1})	$\|M\|^2$ (a.u.)
0	1540.906	0	29581.117	3.774
0	1540.906	1	31559.468	2.364
0	1540.906	2	33380.971	1.016
0	1540.906	3	35051.018	0.389
0	1540.906	4	36572.006	0.145
0	1540.906	5	37942.821	0.055
0	1540.906	6	39157.901	0.022
0	1540.906	7	40204.525	0.009
0	1540.906	8	41054.494	0.004
0	1540.906	9	41650.736	0.002
1	4499.658	0	29581.117	0.874
1	4499.658	1	31559.468	0.736
1	4499.658	2	33380.971	1.926
1	4499.658	3	35051.018	1.599
1	4499.658	4	36572.006	0.946
1	4499.658	5	37942.821	0.491
1	4499.658	6	39157.901	0.243
1	4499.658	7	40204.525	0.119
1	4499.658	8	41054.494	0.058
1	4499.658	9	41650.736	0.025
1	4499.658	10	42002.891	0.012
1	4499.658	12	42159.395	0.002
2	7301.650	0	29581.117	0.070
2	7301.650	1	31559.468	0.883
2	7301.650	2	33380.971	0.005
2	7301.650	3	35051.018	0.766
2	7301.650	4	36572.006	1.289
2	7301.650	5	37942.821	1.158
2	7301.650	6	39157.901	0.811
2	7301.650	7	40204.525	0.504
2	7301.650	8	41054.494	0.285
2	7301.650	9	41650.736	0.139
2	7301.650	10	42002.891	0.071
2	7301.650	11	42136.175	0.002
2	7301.650	12	42159.395	0.010

$^3\Sigma^- - ^3\Pi_0$ transitions (continuation)				
3	9953.124	0	29581.117	0.002
3	9953.124	1	31559.468	0.144
3	9953.124	2	33380.971	0.514
3	9953.124	3	35051.018	0.156
3	9953.124	4	36572.006	0.087
3	9953.124	5	37942.821	0.555
3	9953.124	6	39157.901	0.819
3	9953.124	7	40204.525	0.773
3	9953.124	8	41054.494	0.568
3	9953.124	9	41650.736	0.323
3	9953.124	10	42002.891	0.178
3	9953.124	11	42136.175	0.006
3	9953.124	12	42159.395	0.026
4	12460.153	1	31559.468	0.005
4	12460.153	2	33380.971	0.171
4	12460.153	3	35051.018	0.166
4	12460.153	4	36572.006	0.300
4	12460.153	5	37942.821	0.027
4	12460.153	6	39157.901	0.067
4	12460.153	7	40204.525	0.270
4	12460.153	8	41054.494	0.361
4	12460.153	9	41650.736	0.276
4	12460.153	10	42002.891	0.177
4	12460.153	11	42136.175	0.006
4	12460.153	12	42159.395	0.028
5	14828.776	2	33380.971	0.009
5	14828.776	3	35051.018	0.138
5	14828.776	4	36572.006	0.013
5	14828.776	5	37942.821	0.211
5	14828.776	6	39157.901	0.154
5	14828.776	7	40204.525	0.021
5	14828.776	8	41054.494	0.006
5	14828.776	9	41650.736	0.030
5	14828.776	10	42002.891	0.033
5	14828.776	11	42136.175	0.001
5	14828.776	12	42159.395	0.006
6	17064.943	3	35051.018	0.009
6	17064.943	4	36572.006	0.076
6	17064.943	5	37942.821	0.010
6	17064.943	6	39157.901	0.055
6	17064.943	7	40204.525	0.134
6	17064.943	8	41054.494	0.096
6	17064.943	9	41650.736	0.037
6	17064.943	10	42002.891	0.013
6	17064.943	12	42159.395	0.001
7	19174.511	4	36572.006	0.006
7	19174.511	5	37942.821	0.024
7	19174.511	6	39157.901	0.035
7	19174.511	8	41054.494	0.026
7	19174.511	9	41650.736	0.038
7	19174.511	10	42002.891	0.029
7	19174.511	11	42136.175	0.001
7	19174.511	12	42159.395	0.005
8	21163.200	4	36572.006	0.002

$^3\Sigma^- - ^3\Pi_0$ transitions (continuation)				
8	21163.200	5	37942.821	0.001
8	21163.200	6	39157.901	0.003
8	21163.200	7	40204.525	0.024
8	21163.200	8	41054.494	0.015
8	21163.200	9	41650.736	0.002
9	23036.530	4	36572.006	0.002
9	23036.530	5	37942.821	0.007
9	23036.530	8	41054.494	0.003
9	23036.530	9	41650.736	0.007
9	23036.530	10	42002.891	0.005
10	24799.750	5	37942.821	0.006
10	24799.750	6	39157.901	0.016
11	26457.784	5	37942.821	0.002
11	26457.784	6	39157.901	0.018
11	26457.784	7	40204.525	0.024
12	28015.158	6	39157.901	0.007
12	28015.158	7	40204.525	0.041
12	28015.158	8	41054.494	0.013
12	28015.158	9	41650.736	0.009
12	28015.158	10	42002.891	0.002
13	29475.813	6	39157.901	0.001
13	29475.813	7	40204.525	0.023
13	29475.813	8	41054.494	0.054
13	29475.813	9	41650.736	0.002
13	29475.813	10	42002.891	0.001
14	30843.067	7	40204.525	0.007
14	30843.067	8	41054.494	0.058
14	30843.067	9	41650.736	0.012
14	30843.067	10	42002.891	0.016
14	30843.067	12	42159.395	0.002
15	32119.545	7	40204.525	0.001
15	32119.545	8	41054.494	0.033
15	32119.545	9	41650.736	0.052
15	32119.545	10	42002.891	0.015

10. APPENDIX C: HE-OH$^+(X)$ POTENTIAL ENERGY SURFACE

The He-OH$^+$($^3\Sigma^-$) interaction potential has being calculated on a grid of points in Jacobi coordinates, where r is the intenuclear OH$^+$ distance, R is the distance between He and the center of mass of the OH$^+$, and θ is the angle between the vectors of lengths R and r (with $\theta = 0^\circ$ corresponding to the He-H-O collinear arrangement). *Ab initio* calculations are performed for 57 intermolecular R distances in the range between 2.75 a_0 and 32 a_0 distributed in the vicinity of the minimum with a step of 0.1 a_0 and 0.25 or 0.5 a_0 outside. The angular θ coordinate is represented by a grid of 15 Gauss-Legendre nodes. The intramolecular distance r is varied between 1.7 a_0 and 2.6 a_0 on a grid of 5 radial points, which is enough to describe the first vibrational levels of OH$^+$($^3\Sigma^-$).

We use the spin unrestricted coupled cluster method with single, double and non-iterative triple excitations (UCCSD(T)) (Knowles et al. 1993, 2000) for the calculations of total energies of the ground electronic state of He-OH$^+$, using MOLPRO program (MOLPRO 2010). The system is well described by a single-determinant wave function, therefore we use restricted Hartree-Fock (RHF) calculations as a reference for subsequent UCCSD(T) calculations. We used the augmented correlation-consistent quadruple-zeta (AVQZ) basis set (Dunning & Jr. 1989) of Dunning *et al.* augmented with $3s2p1d$ mid-bond functions (s : $0.553063, 0.250866, 0.117111$, p : $0.392, 0.142$, d : 0.328). The standard Boys and Bernardi (Boys & Bernardi 1970) counterpoise procedure is used to correct the interaction energy for the basis set superposition error (BSSE).

We have used the UCCSD(T) method for the He-OH+ PES instead of MRCI as before for the sole diatom as it avoids the size-consistency problems and recovers larger portion of correlation energy due to the perturbative inclusion of triple excitations, which is important for van der Waals complexes containing helium. The choice of AVQZ+bond functions basis offers good ratio of accuracy (energies can be close to the complete basis set limit) to computational time, as we have more degrees of freedom in comparison to sole OH cation.

The potential is expanded in a series of Legendre polynomials, $V(R,r,\theta) = \sum_{l=0}^{15} v_l(R,r)P_l(\cos\theta)$ in order to represent the potential in the analytical form. The radial expansion coefficients for each r are interpolated along intermolecular distance R using Reproducing Kernel Hilbert space method. The dependence on the r intramolecular distance is obtained by polynomial expansion in a dimensionally reduced $z = (r - r_e)/r_e$ coordinate.

We averaged the three-dimensional (3-D) $V(R,r,\theta)$ PES over the ground vibrational state of the OH$^+$ cation to obtain the $V_0(R,\theta)$ He-OH$^+$ potential that we can use in subsequent scattering calculations. The potential exhibits global minimum at collinear He-H-O geometry for $\theta = 0^\circ$. The well depth of the $V_0(R,\theta)$ potential is $D_e = 729.6$ cm^{-1} located at $R_e = 4.79$ a_0. These values can be compared to potential published almost two decades before by Meuwly and coworkers Meuwly et al. (1998). Meuwly *et al.* reports D_e of 701 cm^{-1} and R_e of 4.83 a_0. These are quite similar values in comparison to result in this work with our potentials being slightly more attractive. The origin of the deep well for this helium complex lies in the fact that OH$^+$($^3\Sigma^-$)'s positive charge acts as an acceptor of the helium electron cloud acting as a donor. This simple model is discussed by Hughes *et al.* in their studies of HeOH$^+$ molecule (Hughes & von Nagy-Felsobuki (1997)). The He atom binds strongly to the protonated side of the OH$^+$ in the entrance channel of reaction to form the strongly bound molecular HeH$^+$ ion. The zero-point dissociation energy of the He-OH$^+$ complex is reported(Meuwly et al. (1998)) to be around 360 cm^{-1}. The D_0 value calculated with our new UCCSD(T) potential is 391 cm^{-1}. This indicates a fair stability of this helium complex.

11. APPENDIX D: HE+OH$^+$ INELASTIC COLLISIONS

As described above, in the OH$^+$($X^3\Sigma^-$) electronic ground state, the rotational levels are split by spin-rotation coupling as previously mentioned in section 2, and the rotational wave functions written for $J \geq 1$ as (Gordy & Cook 1984; Lique et al. 2005):

$$\begin{aligned} |F_1 JM\rangle &= \cos\alpha|N = J-1, SJM\rangle \\ &\quad + \sin\alpha|N = J+1, SJM\rangle \\ |F_2 JM\rangle &= |N = J, SJM\rangle \\ |F_3 JM\rangle &= -\sin\alpha|N = J-1, SJM\rangle \\ &\quad + \cos\alpha|N = J+1, SJM\rangle \end{aligned} \tag{18}$$

where $|N, SJM\rangle$ denotes pure Hund's case (b) basis functions (see Appendix B) and the mixing angle α is obtained by diagonalization of the molecular Hamiltonian. In the pure case (b) limit, $\alpha \to 0$, the F_1 level corresponds to $N = J - 1$ and the F_3 level to $N = J + 1$.

The rotational energy levels of the OH^+ molecule were computed with the use of experimental spectroscopic constants of (Merer et al. 1975).

The quantal coupled equations were solved in the intermediate coupling scheme using the MOLSCAT code (Hutson & Green 1994) modified to take into account the fine structure of the energy levels.

For the OH^+ molecule, an additional splitting of rotational levels exists. The Hydrogen atom possesses a non-zero nuclear spin ($I = 0.5$) so that the energy levels of OH^+ are characterized by the quantum numbers N, J and F, where F results from the coupling of $\vec{J}$ with $\vec{I}$ ($\vec{F} = \vec{J} + \vec{I}$). The hyperfine splitting of the OH^+ levels being very small, the hyperfine levels can be safely assumed to be degenerate as was considered in the transitions treated in the previous section. Then, it is possible to simplify considerably the hyperfine scattering problem. The integral cross sections corresponding to transitions between hyperfine levels of the OH^+ molecules can be obtained from scattering S-matrix between fine structure levels using a recoupling method (Alexander & Dagdigian 1985).

Inelastic cross sections associated with a transition from an initial hyperfine level N, J, F to a hyperfine level N', J', F' were thus obtained as follow :

$$\sigma_{NJF\to N'J'F'} = \frac{\pi}{k^2_{NJF}}(2F'+1)\sum_K \times \left\{ \begin{array}{ccc} J & J' & K \\ F' & F & I \end{array} \right\}^2 P^K(J \to J') \quad (19)$$

The $P^K(J \to J')$ are the tensor opacities defined by :

$$P^K(J \to J') = \frac{1}{2K+1}\sum_{ll'} |T^K(Jl; J'l')|^2 \quad (20)$$

The reduced T-matrix elements (where $T = 1 - S$) are defined by (Alexander & Dagdigian 1983):

$$T^K(Jl; J'l') = (-1)^{-J-l'}(2K+1)\sum_{J_t}(-1)^{J_t}(2J_t+1) \times \left\{ \begin{array}{ccc} l' & J' & J_t \\ J & l & K \end{array} \right\} T^{J_t}(Jl; J'l') \quad (21)$$

where $J_t = J + l$ is the total triatomic angular momentum, and l is the orbital angular momentum quantum number.

The scattering calculations were carried out on total energy, E_{tot}, grid with a variable steps. For the energies below 1000 cm^{-1} the step was equal to 1 cm^{-1}, then, between 1000 and 1500 cm^{-1} it was increased to 10 cm^{-1}, and to 100 cm^{-1} for energy interval from 1500 to 2200 cm^{-1}. In order to ensure convergence of the inelastic cross sections, it is necessary to include in the calculations several energetically inaccessible (closed) levels. At the largest energies considered in this work, the OH^+ rotational basis were extended to $N = 10$ to ensure convergence of the cross sections of OH^+.

REFERENCES

Agúndez, M., & Cernicharo, J. 2006, ApJ, 650, 374.
Agúndez, M., Fonfría, J. P., Cernicharo, J., Pardo, J. R., & Guélin, M. 2008, A&A, 479, 493.
Aleman, I., Ueta, T., Ladjal, D., et al. 2014, ArXiv e-prints, arXiv:1404.2431.
Alexander, M. H. 1985, Chem. Phys., 92, 337.
Alexander, M. H., & Dagdigian, P. J. 1983, J. Chem. Phys., 79, 302.
—. 1985, J. Chem. Phys., 83, 2191.
Aslan, E., Bulut, N., Castillo, J. F., et al. 2012, ApJ, 739, 31.
Benz, A. O., Bruderer, S., van Dishoeck, E. F., et al. 2010, A&A, 521, L35.
Boys, S. F., & Bernardi, F. 1970, Mol. Phys., 19, 553.
Brzozowski, J., Elander, N., Erman, P., & Lyyra, M. 1974, Phys. Scripta, 10, 241.
Burley, J. D., Ervin, K. M., & Armentrout, P. 1987, Int. J. Mass Spect. and Ion Processes, 80, 153.
Cernicharo, J. 2012, in Proceedings of the European Conference on Laboratory Astrophysics, European Astronomical Society Publications Series, ed. C. Stehlé, C. Joblin, & L. d'Hendecourt
Cernicharo, J., Decin, L., Barlow, M. J., et al. 2010, A&A, 518, L136.
Chen, R., & Guo, H. 1996, J. Chem. Phys., 105, 3569.
Christoffel, K. M., & Bowman, J. M. 1983, J. Chem. Phys., 78, 3952.
D. E. Woon and Jr. T. H. Dunning. 1994, J. Chem. Phys., 101, 8877.
Davidson, E. R. 1975, J. Comp. Phys., 17, 87.
de Almeida, A. A., & Singh, P. D. 1981, ApJL, 95, 383, 383
Dubernet, M.-L., Alexander, M. H., Ba, Y. A., et al. 2013, A&A, 553, A50.
Dumouchel, F., Spielfiedel, A., Senent, M. L., & Feautrier, N. 2012, Chem. Phys. Lett., 533, 6.
Dunning, T. H., & Jr. 1989, J. Chem. Phys., 90, 1007.
Etxaluze, M., Goicoechea, J. R., Cernicharo, J., et al. 2013, A&A, 556, A137.
Etxaluze, M., Cernicharo, J., Goicoechea, J. R., et al. 2014, ArXiv e-prints, arXiv:1404.2177
Faure, A., & Tennyson, J. 2001, MNRAS, 325, 443.
Gerin, M., De Luca, M., Black, J., et al. 2010, A&A, 518, L110.
Gioumousis, G., & Stevenson, D. P. 1958, J. Chem. Phys., 29, 294.
Godard, B., & Cernicharo, J. 2013, A&A, 550, A8.
Godard, B., Falgarone, E., Gerin, M., et al. 2012, A&A, 540, A87.
Goicoechea, J. R., Etxaluze, M., Cernicharo, J., et al. 2013, ApJ, 769, L13.
Goldfield, E. M., Gray, S. K., & Schatz, G. C. 1995, J. Chem. Phys., 102, 8807.
Gómez-Carrasco, S., & Roncero, O. 2006, J. Chem. Phys., 125, 054102.
González-Alfonso, E., & Cernicharo, J. 1999, in ESA Special Publication, Vol. 427, The Universe as Seen by ISO, ed. P. Cox & M. Kessler, 325.
González-Alfonso, E., Fischer, J., Bruderer, S., et al. 2013, A&A, 550, A25
González-Lezana, T., Aguado, A., Paniagua, M., & Roncero, O. 2005, J. Chem. Phys., 123, 194309.
Gordy, W., & Cook, R. L. 1984, Microwave molecular spectra, Wileys and sons.
Gray, S. K., & Balint-Kurti, G. G. 1998, J. Chem. Phys., 108, 950.
Gruebele, M. H. W., Müler, R. P., & Saykally, R. J. 1986, J. Chem. Phys., 84, 2489.
Herzberg, G. 1950, Molecular spectra and molecular structure. I. Spectra of diatomic molecules, van Nostrand Reinhold Co. (New York).
Hily-Blant, P., Maret, S., Bacmann, A., et al. 2010, A&A, 521, L52.
Hollenbach, D., Kaufman, M. J., Neufeld, D., Wolfire, M., & Goicoechea, J. R. 2012,ApJ, 105, 754.
Huang, Y., Iyengar, S. S., Kouri, D. J., & Hoffman, D. K. 1996, J. Chem. Phys., 105, 927.
Huang, Y., Kouri, D. J., & Hoffman, D. K. 1994, J. Chem. Phys., 101, 10493.
Hughes, J. M., & von Nagy-Felsobuki, E. I. 1997, J. Phys. Chem. A, 101, 3995.
Hutson, J. M., & Green, S. 1994, MOLSCAT computer code, version 14 (1994), distributed by Collaborative Computational Project No. 6 of the Engineering and Physical Sciences Research Council (UK)
Indriolo, N., Geballe, T. R., Oka, T., & McCall, B. J. 2007, ApJ, 671, 1736.
Indriolo, N., & McCall, B. J. 2012, ApJ, 745, 91.
Knowles, P. J., Hampel, C., & Werner, H.-J. 1993, J. Chem. Phys., 99, 5219.
—. 2000, J. Chem. Phys., 112, 3106.
Krelowski, J., Beletsky, Y., & Galazutdinov, G. A. 2010, ApJ, 719, L20.
Kroes, G. J., & Neuhauser, D. 1996, J. Chem. Phys., 105, 8690.
Langevin, P. 1905, Ann. Chim. Phys., 5, 245.
Larsson, M. 1983, A&A, 128, 291.
Le Bourlot, J., Le Petit, F., Pinto, C., Roueff, E., & Roy, F. 2012, A&A, 541, A76.
Le Petit, F., Nehmé, C., Le Bourlot, J., & Roueff, E. 2006, ApJS, 164, 506, 506
Lefebvre-Brion, H., & Field, R. W. 1986, Perturbations in the Spectra of Diatomic Molecules, Academic Press, London.
Lique, F. 2010, J. Chem. Phys., 132, 044311.
Lique, F., & Kłos, J. 2011, MNRAS, 413, L20.
Lique, F., Spielfiedel, A., Dubernet, M. L., & Feautrier, N. 2005, J. Chem. Phys., 123, 134316.
Lique, F., Toboła, R., Kłos, J., et al. 2008, A&A, 478, 567.
Mandelshtam, V. A., & Taylor, H. S. 1995, J. Chem. Phys., 103, 2903.
Martínez, R., Millán, J., & González, M. 2004, J. Chem. Phys., 120, 4705.
Martínez, R., Sierra, D., & González, M. 2005, J. Chem. Phys., 123, 174312.
Martínez, R., Sierra, J. D., Gray, S. K., & González, M. 2006, J. Chem. Phys., 125, 164305.
Mathis, J. S., Mezger, P. G., & Panagia, N. 1983, A&A, 128, 212.
Merer, A. J., Malm, D. N., Martin, R. W., Horani, M., & Rostas, J. 1975, Can. J. Phys., 53, 251.
Meuwly, M., Meier, J. P., & Rosmus, P. 1998, J. Chem. Phys., 109, 3850.
Miller, W. H. 1974, J. Chem. Phys., 61, 1823.
Möhlmann, G. R., Bhutani, K. K., de Heer, F. J., & Tsurubuchi, S. 1978, Chem. Phys., 31, 273.
MOLPRO. 2010, package of *ab initio* programs written by H.-J. Werner and P. J. Knowles, with contributions from R. D. Amos, A. Berning, D. L.Cooper, M. J. O. Deegan, A. J. Dobbyn, F. Eckert, C. Hampel, T. Leininger, R. Lindh, A. W. Lloyd, W. Meyer, M. E. Mura, A. Nicklaß, P.Palmieri, K. Peterson, R. Pitzer, P. Pulay, G. Rauhut, M. Schütz, H. Stoll, A. J. Stone and T. Thorsteinsson.
Nagy, Z., Van der Tak, F. F. S., Ossenkopf, V., et al. 2013, A&A, 550, A96.
Naylor, D. A., Dartois, E., Habart, E., et al. 2010, A&A, 518, L117.
Neufeld, D. A., Goicoechea, J. R., Sonnentrucker, P., et al. 2010, A&A, 521, L10.
Neufeld, D. A., González-Alfonso, E., Melnick, G., et al. 2011, ApJ, 727, L29.
Neuhauser, D. 1994, J. Chem. Phys., 100, 9272.
Pilleri, P., Fuente, A., Gerin, M., et al. 2014, A&A, 561, A69.
Porras, A. J., Federman, S. R., Welty, D. E., & Ritchey, A. M. 2014, ApJ, 781, L8.
Roueff, E., & Lique, F. 2013, Chemical Reviews, 113, 8906.
Schöier, F. L., van der Tak, F. F. S., van Dishoeck, E. F., & Black, J. H. 2005, A&A, 432, 369.
Skouteris, D., Castillo, J., & Manolopoulos, D. E. 2000, Comp. Phys. Commun., 133, 128, 128
Smith, L. N., Malik, D. J., & Secrest, D. 1979, J. Chem. Phys., 71, 4502.
Spoon, H. W. W., Farrah, D., Lebouteiller, V., et al. 2013, ApJ, 775, 127.
Toboła, R., Dumouchel, F., Kłos, J., & Lique, F. 2011, J. Chem. Phys., 134, 024305.
Troutman, M. R., Hinkle, K. H., Najita, J. R., Rettig, T. W., & Brittain, S. D. 2011, ApJ, 738, 12.
van der Tak, F. F. S., Black, J. H., Schöier, F. L., Jansen, D. J., & van Dishoeck, E. F. 2007, A&A, 468, 627.
van der Tak, F. F. S., Nagy, Z., Ossenkopf, V., et al. 2013, A&A, 560, A95.
van der Werf, P. P., Isaak, K. G., Meijerink, R., et al. 2010, A&A, 518, L42.
van Dishoeck, E. F., Kristensen, L. E., Benz, A. O., et al. 2011, PASP, 123, 138.
Whiting, E. E., & Nicholls, R. W. 1974, Astrophys. J. Supp. Series, 27, 1, 1
Whiting, E. E., Schadee, A., Taum, J. B., Hougen, J. T., & Nicholls, R. W. 1980, J. Mol. Spect., 80, 249.
Wyrowski, F., van der Tak, F., Herpin, F., et al. 2010, A&A, 521, L34+.
Xu, W., Li, W., Lv, S., et al. 2012, J. Phys. Chem. A, 116, 10882.
Zanchet, A., Agúndez, M., Herrero, V. J., Aguado, A., & Roncero, O. 2013a, AJ, 146, 125.
Zanchet, A., Godard, B., Bulut, N., et al. 2013b, ApJ, 766, 80.
Zanchet, A., Roncero, O., González-Lezana, T., et al. 2009, J. Phys. Chem. A, 113, 14488.
Zare, R. 1988, Angular Momentum, John Wiley and Sons, Inc.
Zhang, D. H., & Zhang, J. Z. H. 1994, J. Chem. Phys., 101, 3672.